

Cyanographene and Graphene Acid - Emerging Derivatives Enabling High-Yield and Selective Functionalization of Graphene

Aristides Bakandritsos,[†] Martin Pykal,[†] Piotr Blonski,[†] Petr Jakubec,[†] Demetrios D. Chronopoulos,[†] Kateřina Poláková,[†] Vasilios Georgakilas,[‡] Klára Čépe,[†] Ondřej Tomanec,[†] Václav Ranc,[†] Athanasios B. Bourlinos,^{§,†} Radek Zbořil,^{†} Michal Otyepka^{†*}*

[†] Regional Centre for Advanced Technologies and Materials, Department of Physical Chemistry, Faculty of Science, Palacký University Olomouc, 17. listopadu 1192/12, 771 46 Olomouc, Czech Republic

[‡] Department of Materials Science, University of Patras, Patras, Greece

[§] Physics Department, University of Ioannina, Ioannina, Greece

Methods

Reagents and materials. NaCN (p.a. $\geq 97\%$), graphite fluoride (>61 wt.% F, $C_1F_{1.1}$), NaOH concentrate (for preparing 1 L of a 0.1 M standard solution), HCl concentrate (for preparing 1 L of a 0.1 M standard solution), NaOH (reagent grade, $\geq 98\%$, pellets), 2,2'-(Ethylenedioxy)bis(ethylamine) (98%), 2-(2-aminoethoxy)ethanol (98%), cysteamine hydrochloride ($\geq 97\%$), N-(3-Dimethylaminopropyl)-N'-ethylcarbodiimide hydrochloride (EDC, $\geq 99.0\%$), ethyl cyano(hydroxyimino)acetate (oxyma pure), cysteamine hydrochloride ($\geq 97\%$), dimethyl sulfoxide (DMSO, anhydrous, $\geq 99.9\%$), potassium hexacyanoferrate(II) and potassium hexacyanoferrate(III) were purchased from Sigma-Aldrich. Acetone (pure), ethanol (absolute) and potassium chloride were purchased from Penta. Amine free dimethylformamide (DMF), nitric acid (Analupure®, 65%) were obtained from Lach-Ner. All aqueous solutions were prepared with ultrapure water ($18\text{ M}\Omega\text{ cm}^{-1}$).

Structural and physicochemical characterization. FT-IR spectra were recorded on an iS5 FTIR spectrometer (Thermo Nicolet) using the Smart Orbit ZnSe ATR accessory. Briefly, a droplet of an ethanolic dispersion of the relevant material was placed on the ZnSe crystal and left for ethanol to dry and form a film. Spectra were then acquired by summing 52 scans, using nitrogen gas flow through the ATR accessory. ATR and baseline correction were applied to the collected spectra. Raman spectra were recorded on a DXR Raman microscope using the 532 nm excitation line of a diode laser. A combined NTEGRA Spectra system (NT-MDT, Russia) was used to characterize the samples' topography (HA-NC tips, mica substrate). The spectra were accumulated for 600 s (with an exposure time of 1s) using a $50\text{ }\mu\text{m}$ slit, a 600 lines mm^{-1} gating, and a thermoelectrically cooled detector. X-ray photoelectron spectroscopy (XPS) was carried out with a PHI VersaProbe II (Physical Electronics) spectrometer using an Al K α source (15 kV, 50 W). The obtained data were evaluated with the MultiPak (Ulvac - PHI, Inc.) software package.

Electron microscopy images were obtained with TEM JEOL 2010 with LaB6 type emission gun, operating at 160 kV. STEM-HAADF (high-angle annular dark-field imaging) analyses for EDS (Energy-dispersive X-ray spectroscopy) mapping of elemental distributions on the products were performed with a FEI Titan HRTEM microscope operating at 80 kV. For these analyses, a droplet of an aqueous dispersion of the material under study with a concentration of $\sim 0.1\text{ mg mL}^{-1}$ was deposited on a carbon-coated copper grid and slowly dried at laboratory temperature for 24 hours to reduce its content of adsorbed water.

Thermal analyses were performed with an STA449 C Jupiter–Netzsch instrument at a heating rate of $5\text{ }^{\circ}\text{C min}^{-1}$, under an N_2 flow in the sample compartment. The masses of released

gases in the range of 12–60 m/z were determined with a QMS 403 Aëolos instrument (Netzsch), starting at 100 °C to avoid overloading the spectrometer with adsorbed water.

Dynamic Light Scattering (DLS) was performed on aqueous dispersions of $\sim 0.1 \text{ mg mL}^{-1}$. Electrokinetic measurements for the determination of the particles' mobility and zeta-potential (ζ_p) were performed with a Malvern ZetaSizer Nano instrument. DLS was performed using the same instrument, where scattered light was collected at a fixed angle of 173°. The reported hydrodynamic diameters (D_h) are the means of 3 measurements and each measurement was the sum of 12 correlograms and fitting procedures. Cumulants analysis was applied and the reported average D_h values are z-average means. The reported polydispersity index (PDI) values, which range between 0 for an ideally monodispersed sample to 1 for a system with very broad size distribution, were derived using the equation $\text{PDI} = \sigma^2/D_h^2$, where σ is the standard deviation of the distribution in nm.

For the purpose of titration, the material was washed with acidified water (pH = 2) to ensure protonation of the carboxyl groups. It was then washed with ultrapure water to remove excess H_3O^+ until the system's conductivity was stabilized. Then it was suspended in 4 ml of water (total final volume) and titrated with 0.1 M standard NaOH solution. All water used was degassed by boiling for 4 h.

Polarized optical microscopy was performed on an Olympus IX70 inverted optical microscope, using the XL-WPO polarizer installed in the system. A droplet of an aqueous dispersion of graphene acid (2.5 mg mL^{-1}) was deposited on a microscope glass slide and left to dry covered inside a plastic petri dish. To slow down the evaporation of the water and increase the time available for crystallization, several drops of water were deposited on the bottom of the petri dish.

Cytocompatibility studies. Cytocompatibility experiments were performed with NIH/3T3 (mouse fibroblast cells) and HeLa (human cervical cancer cells) cell lines, purchased from ATCC (USA) and cultivated in low glucose Dulbecco's Modified Eagle medium (DMEM, Life Technologies) at 37 °C under a 5% CO_2 enriched atmosphere. For all *in vitro* tests, NIH/3T3 and HeLa cells ($5 \cdot 10^4$ cells/well) were seeded in 24-well plates and incubated overnight to allow the cells to attach to the wells' surfaces. The cells were then exposed to G-COOH at various concentrations for 24 hours (for ROS measurement, live/dead analysis, and optical imaging) or for 3 hours for ROS kinetics measurements.

Cell viability analysis was performed using a BD FACSVerse flow cytometer (BD Biosciences, USA). After 24 h of incubation, the supernatant was removed and cells were gently washed with PBS solution (0.1M, pH 7.4). Cells were then harvested with trypsin (0.25% in EDTA, Sigma Aldrich), transferred to FACS tubes (BD Biosciences, USA), centrifuged (1600 rpm for 5 min), and the pellet was again washed with PBS. After that, the cells were resuspended in 300 μl of

DMEM medium. Viability analysis of the treated cells was performed with propidium iodide (PI, Sigma Aldrich) as a fluorescent live/dead indicator. This assay has been utilized to quantitate apoptotic cell death. Cells were incubated with 5 μl propidium iodide solution (1 mg mL^{-1}) for 5 min, and the fluorescence (indicating cell death) was determined using flow cytometry at $\lambda_{\text{ex}} = 488$ nm and $\lambda_{\text{em}} = 620$ nm. The whole experiment was performed three times; the variation between runs is indicated by the error bars in the relevant plots .

ROS production was measured in parallel to the live/dead flow cytometer analysis. NIH/3T3 and Hela cells were treated with 12.5–750 $\mu\text{g mL}^{-1}$ of G-COOH and incubated for 24 h. After incubation, the growth medium (DMEM) containing G-COOH was removed from the plate and adherent cells were washed twice with fresh medium. Then 2 μl of a fluorescent ROS probe (General Oxidative Stress Indicator CM-H2DCFDA, Life Technologies), which was pre-dissolved in 123 μl DMSO (500 mM) was added to each well. The plate was placed in a CO_2 incubator for 20 min and the fluorescent signal was measured using an Infinite PRO M200 microplate reader (Tecan, Austria) with excitation/emission wavelengths of 505/529 nm. ROS generation was also investigated observed in a ROS kinetic study in which cultivated cells were treated with 12.5, 50, 200 or 400 $\mu\text{g mL}^{-1}$ of G-COOH and 2 μl of the ROS probe was added to each well immediately after the treatment. The quantity of oxygen radicals generated was then measured every 10 min over 3 hours. These measurements were performed three times for every concentration of G-COOH in two independent experiments.

Cell uptake analysis and cell imaging after 24 hours and 4 days of incubation was performed using an IX70 optical microscope (Olympus). Before imaging, the cells were gently washed twice and resuspended in phosphate buffered saline solution (PBS, 0.1M, pH 7.4).

Sheet resistance and electrochemical measurements. The sheet resistance measurements were performed using a Keithley 2401 multimeter and the four-probe technique. The G-GOOH and G.O. samples were deposited as circular spots (mean diameter ~ 0.2 cm) on common paper. The thickness of the film was estimated to 7 μm based on the volume and the surface area of the deposited material and on mass of the material used. GO was obtained according to literature procedures,¹ after one time treatment with HNO_3 and NaClO_3 . Cyclic voltammetry (CV) and Electrochemical impedance spectroscopy (EIS) were carried out with a Metrohm Autolab PGSTAT128N instrument (Metrohm Autolab B.V., Netherlands) controlled with the NOVA software package (version 1.11.2) in a conventional three electrode setup at room temperature (22 ± 2 °C). Platinum wire was used as an auxiliary electrode, an Ag/AgCl (3M KCl) electrode was used as a reference electrode, and glassy carbon electrodes (GCE) served as working electrodes. All EIS spectra were recorded at 5 mV amplitude over the frequency range 0.1 Hz to 100 kHz in 0.1 mol L^{-1} KCl solution in the

presence of 5 mmol L⁻¹ [Fe(CN)₆]^{3-/4-} as a redox probe. Data obtained for the bare GCE were fitted using the equivalent Randles circuit, where R_s , is the solution resistance; CPE, constant phase element, R_{ct} , charge transfer resistance and the Z_w diffusion is known as Warburg impedance (Supplementary Fig. 8b). A constant phase element was used to account for interfacial irregularities such as roughness, porosity and/or changes in electrode geometry.^{2,3} The results were fitted using an extended Randles equivalent circuit featuring a constant phase element, charge transfer resistance, R_{ct} and Warburg impedance Z_w . An additional RC circuit in parallel consisting of GCE/modifier interface resistance R_{int} and GCE/modifier interface capacitance C_{int} was connected in series to the Randles circuit. R_s represents the electrolyte's resistance (Figure S11c).

Computational Details. Plane-wave density functional theory (PW-DFT) calculations were performed with the Perdew, Burke, and Ernzerhof (PBE)⁴ exchange and correlation functional and projected augmented wave potentials (PAW)^{5,6} representing atomic cores, as implemented in the Vienna ab initio simulation package (VASP).^{6,7} The wave functions were expanded in the PW basis set with a cutoff of 600 eV. Brillouin zone integrations were performed using a $10 \times 10 \times 1$ Γ -centered Monkhorst-Pack k -point mesh per conventional 4×3 rectangular cell containing 48 carbon atoms. An extensive study of structural and electronic properties of both CN and COOH functionalized graphene was accomplished. Up to eight functional groups per computational cell were considered. At each coverage, several tens of possible arrangements of CN and COOH on the pristine graphene layer were taken into account and both possible directions of -CN and -COOH adsorption were also considered, *i.e.*, under (bottom) and above (top) the graphene plane. The lowest-energy GS arrangement found at a low coverage (*ca.* 2.1%) was used to generate a starting configuration of a higher coverage (*i.e.*, 4.2% starting from 2.1%) by adding a single group on-top of sp^2 hybridized carbon atom neighboring to sp^3 C atoms. In the next step, this additional group was put on-top of next-nearest C atoms, and so forth (Figure S14). This gradual process allowed us to monitor the total-energy changes and identification of the most plausible (lowest in energy) structures. This procedure was repeated for each coverage. In addition, at each coverage, several other unique configurations with more uniform distribution of CN and COOH in the cell were also considered. The most stable adsorption positions were the top-bottom configurations on-top of neighboring C atoms, where the carboxyl groups tended to form chains over the surface (Figure S15). Cyanide groups exhibited similar tendency only up to ~8% concentration, whereas above this threshold -CN tended to occupied positions on C atoms belonging to the same hexagonal ring (Figure S16). A full structural optimization was performed using a quasi-Newton algorithm until the residual atomic forces were below 25 meV Å⁻¹. Simultaneously, the electronic degrees of freedom were converged to an energy of less than 10⁻⁶ eV.

Molecular dynamics simulations were performed using GROMACS 4.5.⁸ Carbon parameters for graphene were taken from the literature⁹ and the SPC/E¹⁰ water model was used. A 2 fs step was used in all simulations. In the simulations, the system was initially thermalized using the V-rescale method¹¹ with a 0.1 ps time constant and the semi-isotropic Berendsen barostat.¹² Then the system was equilibrated (10 ns) at a temperature of 300 K and 1 bar pressure. The subsequent production run (20 ns) was carried out in the NVT ensemble. Bonds involving hydrogen were constrained using the LINCS algorithm.¹³ Electrostatic interactions were treated using the Particle-Mesh Ewald (PME) method with a real-space cutoff of 1 nm. A stack of 4 functionalized graphene flakes (4.1×4.2 nm; capped with hydrogens) was immersed in a $10 \times 10 \times 10$ nm rectangular box with periodic boundary conditions in all three dimensions. Several starting geometries (COOH groups on the edges and, on the surface, QM ground state) and coverage percentages (23, 29 and 35.4%) were considered. The partial charges of the functional groups were derived according the RESP procedure¹⁴ on a small system (COOH functionalized pyrene). To simulate the high pH environment 55% of the total functional groups were deprotonated, and the net charge was balanced with Na^+ ions. All figures were rendered using PyMOL¹⁵.

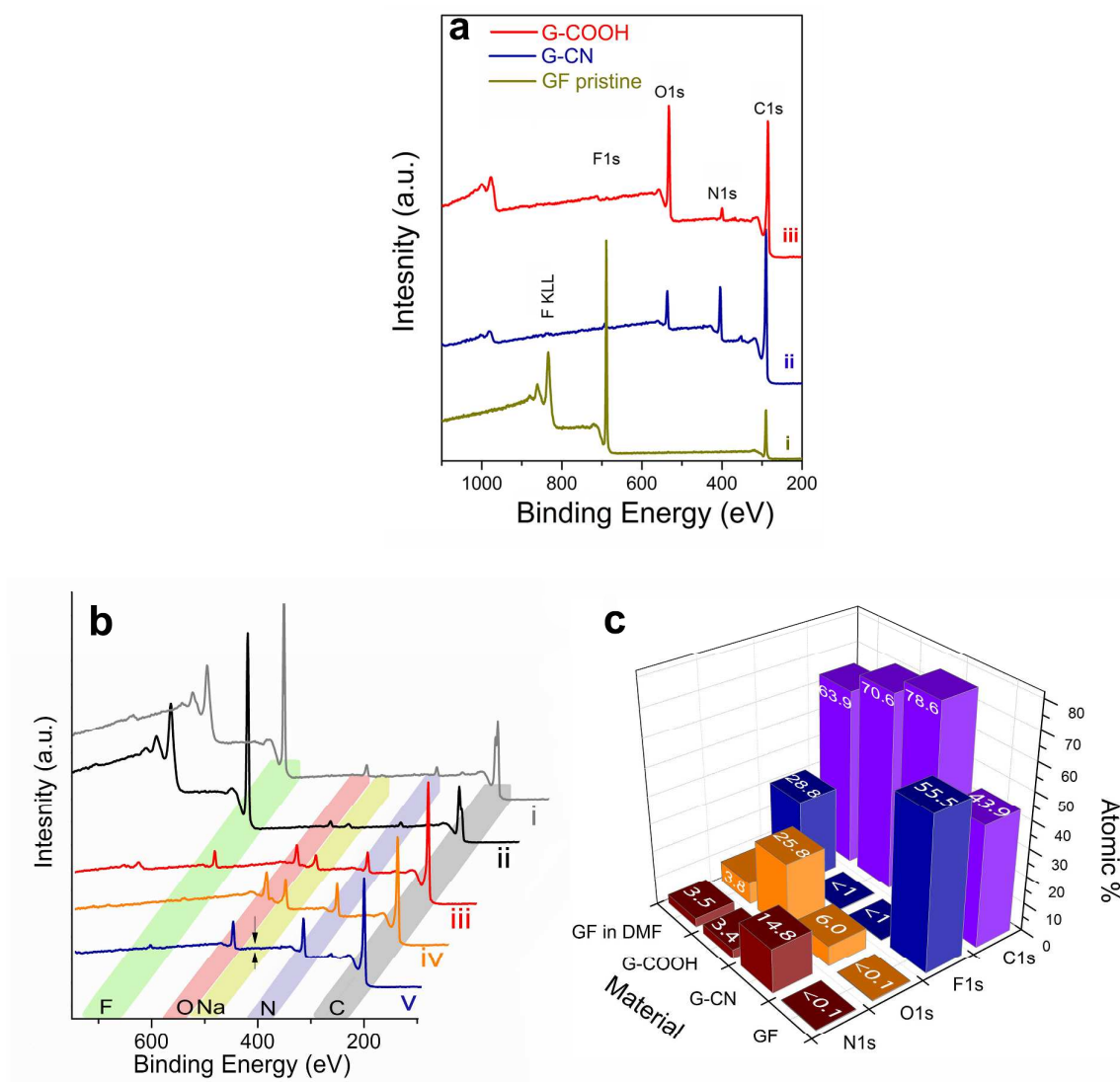


Figure S1. a) Survey XPS of graphite fluoride (*i*, GF), cyanographene (*ii*, G-CN) and graphene acid (*iii*, G-COOH). **b)** XPS spectrum of GF treated in DMF at 130 °C for 24 h (*i*, control sample) showing the presence of N and O impurities in the sample. XPS spectra of FG reaction with NaCN in DMF at 130 °C at various time points (spectra *ii-iv*), showing O, N and Na atoms increasing with the course of the reaction, and the total elimination of F atoms at the end of the reaction (spectrum *iv*). The final G-CN product (spectrum *v*), after treatment with acidified water of pH=4 (HCl used for acidification) verified the complete removal of Na⁺ (through cation exchange with protons), without any change in the content of nitrogen. Na cations in the product *iv* are considered as counterions of the G-CN colloidal particles, whose ζ_p was measured -30 mV (see experimental part in the main manuscript). If cyanides were simply absorbed from the NaCN precursor, then they should have also been washed away along with the Na cations. Another reason which indirectly proves the covalent attachment of the nitrile groups is the fact that at such acidic pH of 4 the equilibrium reaction $\text{NaCN} + \text{HCl} \rightleftharpoons \text{NaCl} + \text{HCN}$ is largely shifted to the right (HCN production). HCN has a boiling

point of 25 °C, therefore during these acidic washing steps through centrifugation, any HCN would have been evaporated or there would be no possibility to detect CN ions under the high vacuum of XPS, or in the dried powder prepared for FT-IR. In order to further support the highly unlikely scenario of CN^- absorption, we performed DFT-D3 calculations and estimated the binding energy of cyanide ions to coronene (as a graphene model), which was found too low (-0.7 kcal/mol). **c)** Atomic contents of elements based on HR-XPS analysis for the control sample (GF in DMF), pristine GF and from the products G-CN and G-COOH. The atmosphere, the high content of water in the hygroscopic NaCN precursor and the reaction solvent (DMF) are potential sources of background oxygen and nitrogen in the samples. When calculating the functionalization degrees of the products, the background atomic contents of O and N were taken into consideration. Specifically, the O (6 at.%) found in G-CN and the N (~3.4 at.%) found in G-COOH and the control sample (which was derived by heat-treating GF in DMF) were regarded as contaminants. Therefore, the CN content of G-CN was assumed to equal its true N content (*i.e.*, 11.4 at.%, after subtraction of the 3.4 at.% background N). The -COOH content in G-COOH, was estimated to be 9.3 at.% on the basis of the deconvoluted C1s spectrum and the component ascribed to the O-C=O carbons (Fig. 2b,ii). The oxygen content of G-COOH is 25.8 at.%; after subtracting the background oxygen level observed in G-CN of 6 at.%, this becomes 19.8 at.%, which is, as expected, almost twice the value for carboxylate carbons. It is noted that the oxygen content in G-CN is higher than in the control sample (GF in DMF), because the NaCN used for obtaining G-CN is highly hygroscopic, thus introducing significant amount of water molecules in the reaction. Finally we should note that these contaminations are considered not as simply absorbed species on the samples, since exhaustive washings have been performed with solvents with different polarities (DMF, DCM, EtOH, acetone, and H_2O) in order to secure the removal of any non-covalently attached species.

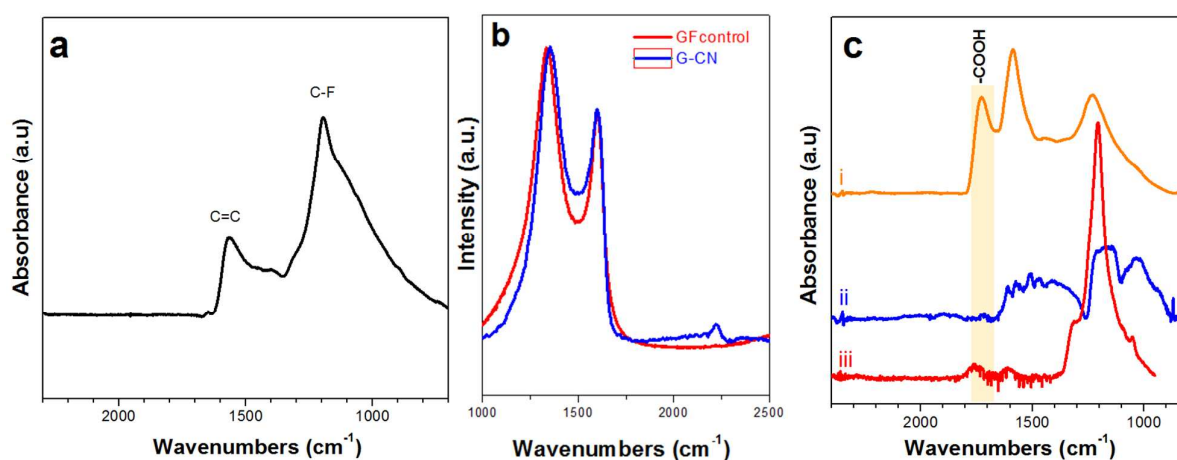


Figure S2. a) FT-IR spectrum of the control sample (GF treated in DMF for 24 h at 100 °C), showing the appearance of the C=C double bond. The C=C and C-F band ratio in this sample is similar to the G-CN intermediate shown in the main manuscript in Figure 1a, spectrum v. The reduction in the fluoride content is quantitatively estimated from the XPS of the control sample shown in Figure S1 b and c. The defluorination is

attributed to reductive defluorination induced by the relatively electron rich nitrogen atom of DMF. It has been previously reported that N containing solvents such as DMF and NMP may exert such effect in fluorographene.¹⁶ **b)** Raman spectrum of the control sample. The G-CN is also included here for comparison. The spectra display identical I_D/I_G intensity ratios and similarly very broad (unresolved) bands. As discussed in the manuscript, G-CN is highly functionalized (~15 % degree of functionalization). Similarly highly functionalized is the control sample, since it contains 28 % of fluorides and thus sp^3 carbons bonded to F atoms. The I_D/I_G intensity ratio is not a linear function of the functionalization degree, and initially increases and then drops above a certain point of functionalization. From that point over there is very high broadening of the bands and the intensity ratio is not indicative any more of the functionalization degree (*refs 37 and 38 in the manuscript*). **c)** FT-IR spectra of the G-COOH product (spectrum *i*) compared with those from the identical treatment of graphite (spectrum *ii*) and the starting GF (spectrum *iii*). The results underline the dramatic differences regarding the COOH presence, providing further evidence that the acidic treatment in G-CN results to hydrolysis and not to oxidation of the carbon lattice. In addition to that, if there was oxidation of the carbon lattice, there should be reduction of the sp^2 carbon component in the C1s HR-XPS spectra of G-COOH, which was not observed based on the deconvolution results for G-CN and G-COOH.

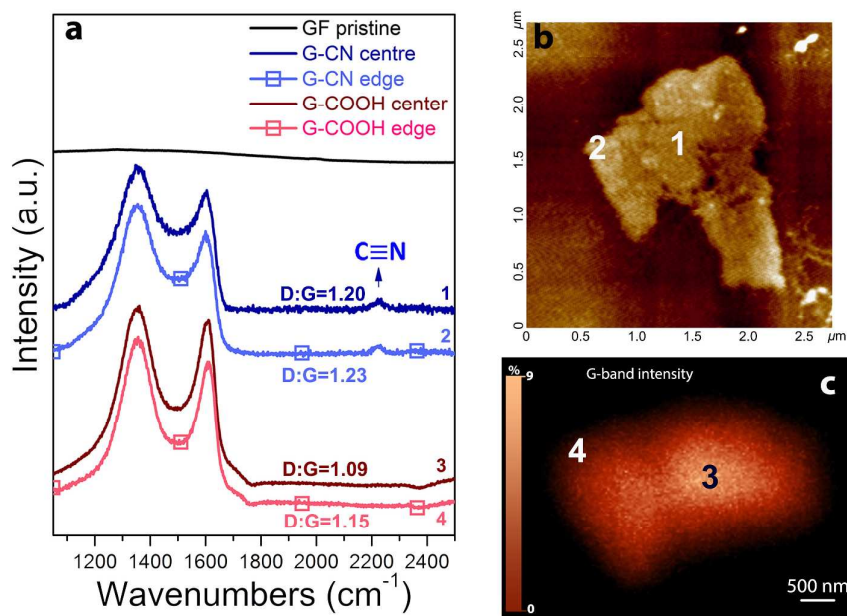


Figure S3. Raman spectra of the starting material and products. **a)** The Raman spectrum of pristine GF is practically featureless, whereas its two derivatives have broad D and G bands and high I_D/I_G ratios. Measurements performed with a Raman-coupled AFM microscope indicate that the values of the latter parameter in the centers of the flakes and at their edges are very similar, demonstrating the homogenous distribution of CN/COOH groups within G-CN/G-COOH sheets. **b)** AFM image of the G-CN flake showing the regions of Raman spectra acquisition. **c)** Raman map from a G-COOH flake based on the intensity of the

G-band and showing the regions of Raman spectra acquisition. The color gradient represents intensity differences up to 9%, which in turn correspond to I_D/I_G ratios of 1.09 for the edge and 1.15 for the center of the flake.

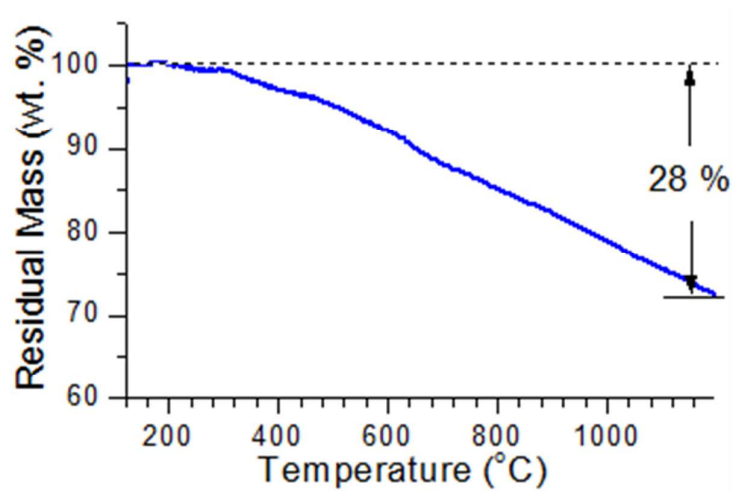


Figure S4. TGA analysis of the G-CN product. Mass loss starts above 200 °C supporting the covalent nature of the –CN functionalities, to which the mass loss is attributed.

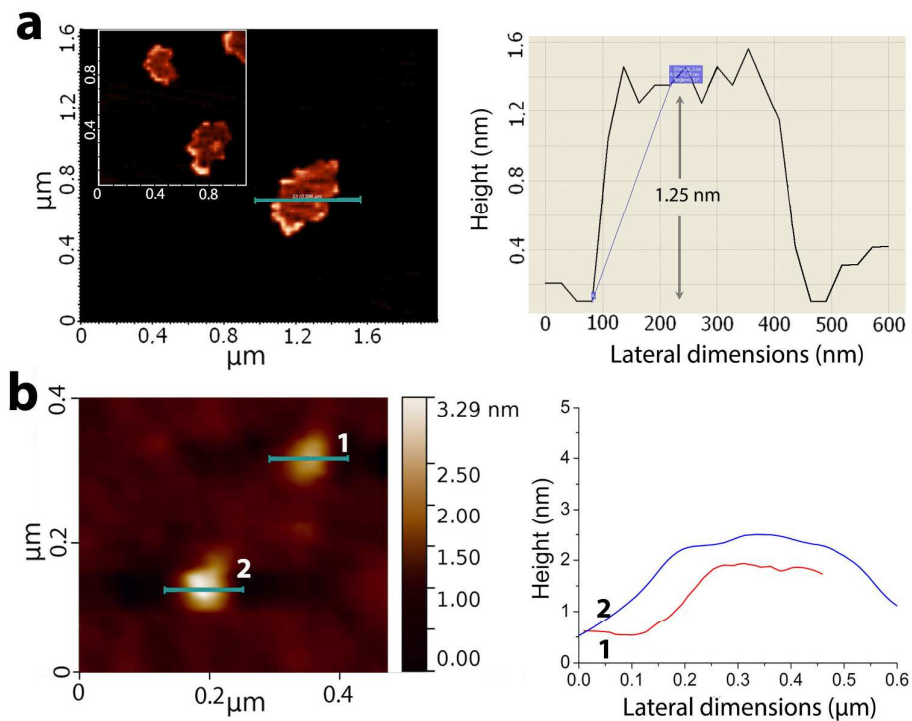


Figure S5. AFM images corroborating the single or few-layer nature of the graphene derivatives. **a)** G-CN and **b)** G-COOH flakes with height profiles.

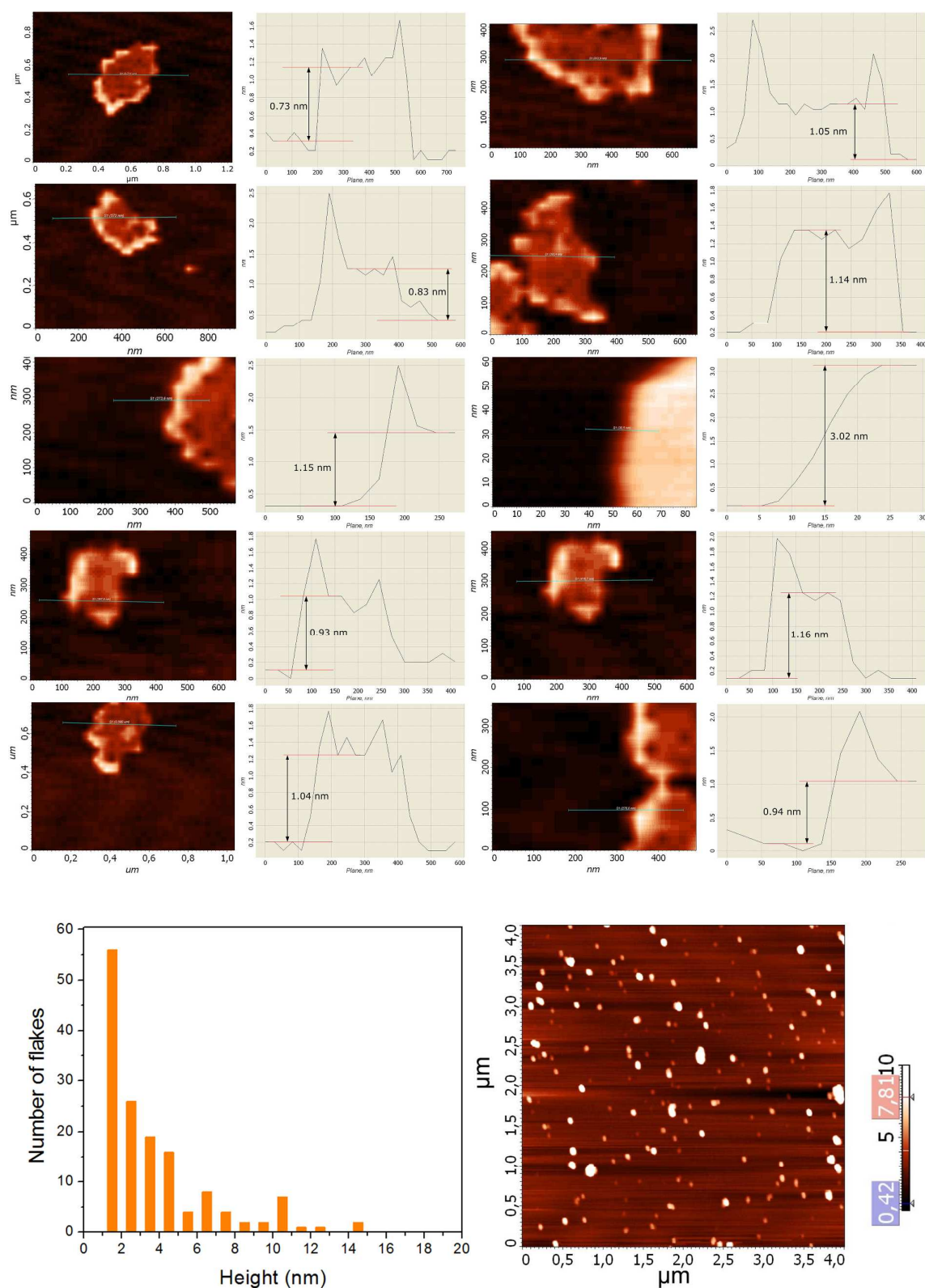


Figure S6. AFM images and height profiles obtained from the G-CN product. At the bottom row a histogram of the height distribution is depicted (from 150 flakes) along with an indicative AFM image from which the histogram was prepared. These results corroborate the single or few-layer nature in G-CN.

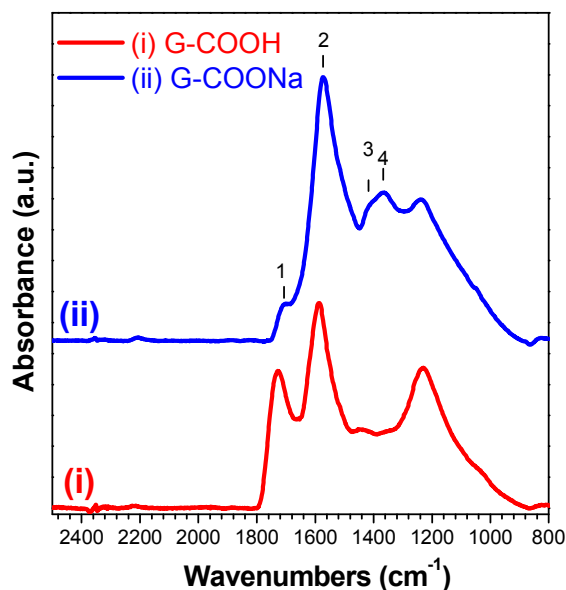


Figure S7. FT-IR spectra of G-COOH and G-COO⁻ Na⁺. **(i)** The FT-IR spectrum of G-COOH features the characteristic asymmetric C=O stretching band of carboxylic acids (band #1). **(ii)** The FT-IR spectrum of G-COONa exhibits pronounced suppression of band #1 and strengthening of bands 2, 3 and 4. (band #2: asymmetric -COO⁻ stretching in carboxylic salts; bands #3 and #4: symmetric C=O stretching in carboxylic salts). The C=C stretching band in the G-COOH spectrum (see also Figs. 1a and 2a) largely overlaps with the asymmetric COO⁻ stretching band (band #2). Comparisons of the FT-IR spectra of graphene acid and sodium graphene carboxylate demonstrated that the FT-IR bands are due to carboxyls rather than to ketones or other oxygen containing chemical groups.

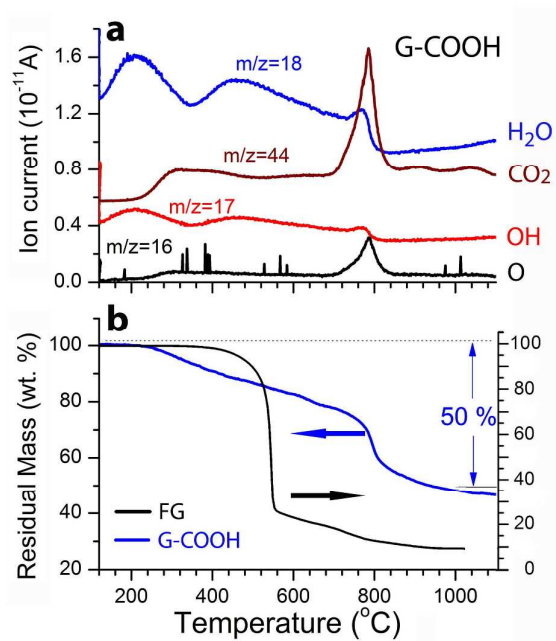


Figure S8. Thermogravimetric (TGA) and evolved gas analyses (EGA) illustrate the different properties of the parent material GF and G-COOH, and the latter material's high degree of functionalization. **a)** EGA results for G-COOH in N_2 . **b)** G-COOH displays a mass-loss of $\sim 30\%$ up to ~ 800 $^{\circ}C$, which is consistent with the 32 wt.% mass content of $-COOH$ groups suggested from the XPS analysis. The evolution of oxygen ($m/z=16$) at ~ 800 $^{\circ}C$ originating from the material's oxygen functionalities, lead to oxidative combustion and decomposition of lattice-carbon atom above 800 $^{\circ}C$.

Table S1. Degrees of covalent graphene functionalization achieved in earlier studies and in the present work, and the methods used to achieve that functionalization. The degree of functionalization was estimated from the experimental data presented in each reference.

Reaction path	Functionalization	Reference
	Degree (%)	
Aryl diazonnium salt	1.8	17
Aryne cycloaddition	6	18
1-3 dipolar cycloaddition of a modified amino acid	0.8	19
Nitrene cycloaddition of azidophenylalanine	7.7 ^a	20
Bingel reaction with malonate	2.3	21
Aryl diazonnium salt	1.2	22
Force accelerated diels-alder cycloaddition	1.3	23
Electrophilic addition of phenyliodide	2.9	24
Aryl diazonnium salt	2-5	25
Ion exposure to azopyridinium	3	26
Cyanographene derivative from nucleophilic substitution of FG	15	this work
Graphene-acid derivative from acidic hydrolysis of cyanographene	13	this work

^a Singlet phenyl nitrene primarily isomerizes to the corresponding cyclic ketenimine, which then reacts with the phenyl azide itself to form a polymeric tar.^{27,28} It is therefore highly likely that multiple layers, rather than a single layer of phenyl azide, was deposited on graphene resulting in an apparent high degree of functionalization.

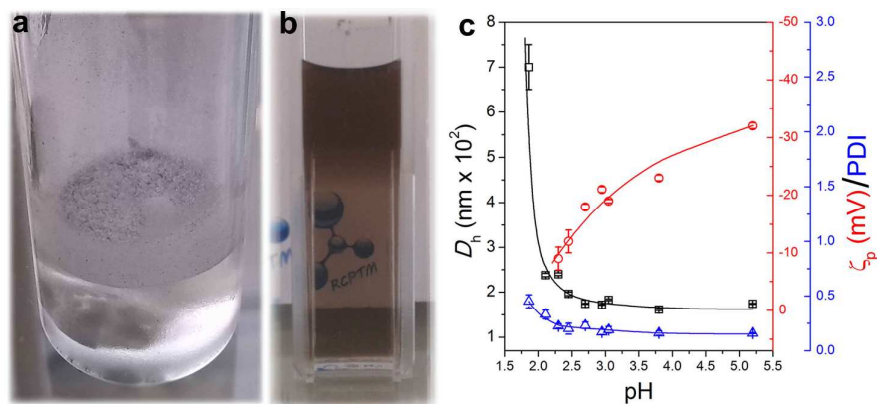


Figure S9. The very hydrophobic nature of pristine FG is reversed after functionalization. **a)** FG in water. **b)** G-COOH in water. **c)** The pH dependence of the ζ_p , D_h and PDI of G-COOH.

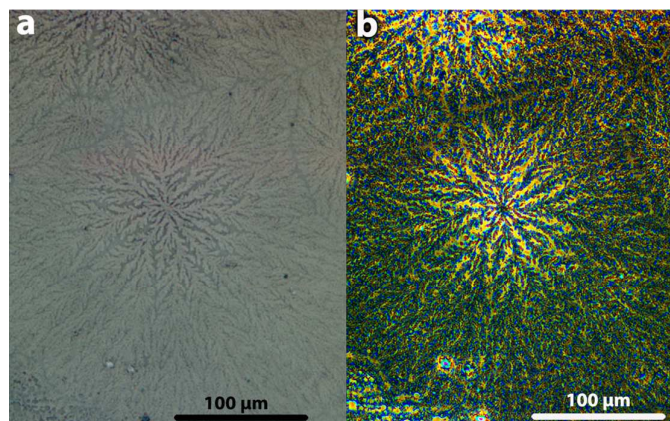


Figure S10. Assembly of graphene acid into organized 3-D superstructures. **a)** G-COOH observed through an optical microscope without polarizers after slow drying from a 0.3 mg mL^{-1} suspension of $\text{pH} = 8$ (pH adjusted with 0.1 M NaOH). **b)** The same sample observed through the same microscope with polarizers.

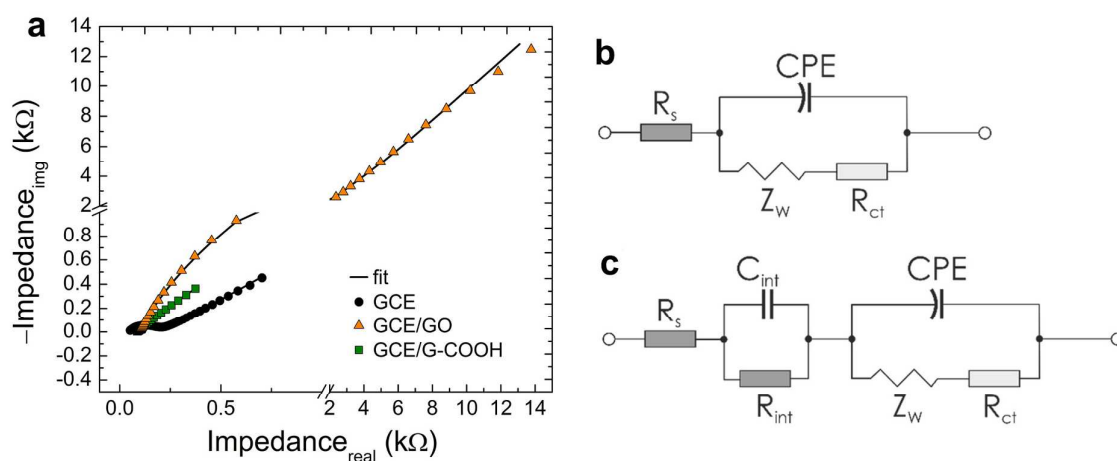


Figure S11. Electrochemical impedance spectroscopy (EIS) measurements demonstrate the conductive nature of graphene-acid. **a)** Nyquist plots for a bare glassy carbon electrode GCE and electrodes modified with GO or G-COOH. GO was prepared according to literature procedures¹, after one time treatment with HNO_3 and NaClO_3 . **b)** Randles equivalent circuit for data fitting and **c)** Extended Randles equivalent circuit for data fitting.

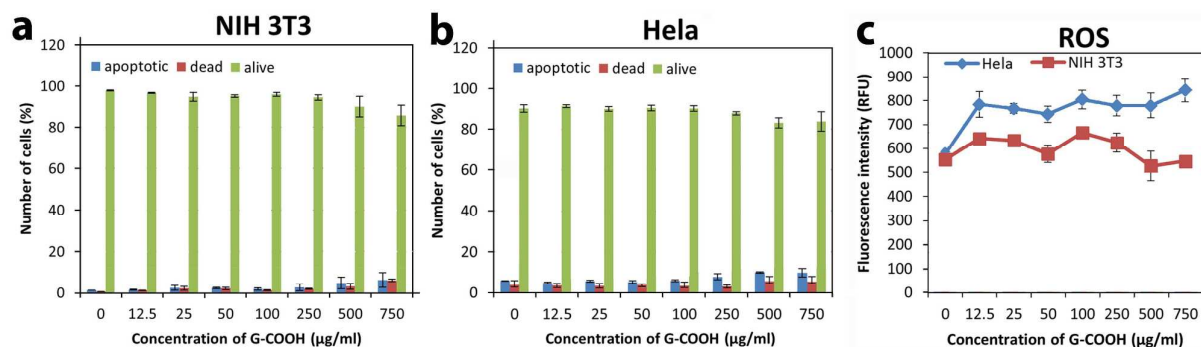


Figure S12. Cytocompatibility assessment for G-COOH. Flow cytometric cell viability measurements for **a)** NIH 3T3 and **b)** HeLa cells after 24 hours' incubation with various concentrations of G-COOH. **c,** Reactive oxygen species levels in NIH 3T3 and HeLa cells after 24 hours of G-COOH incubation compared to control cells. (RFU: relative fluorescence units).

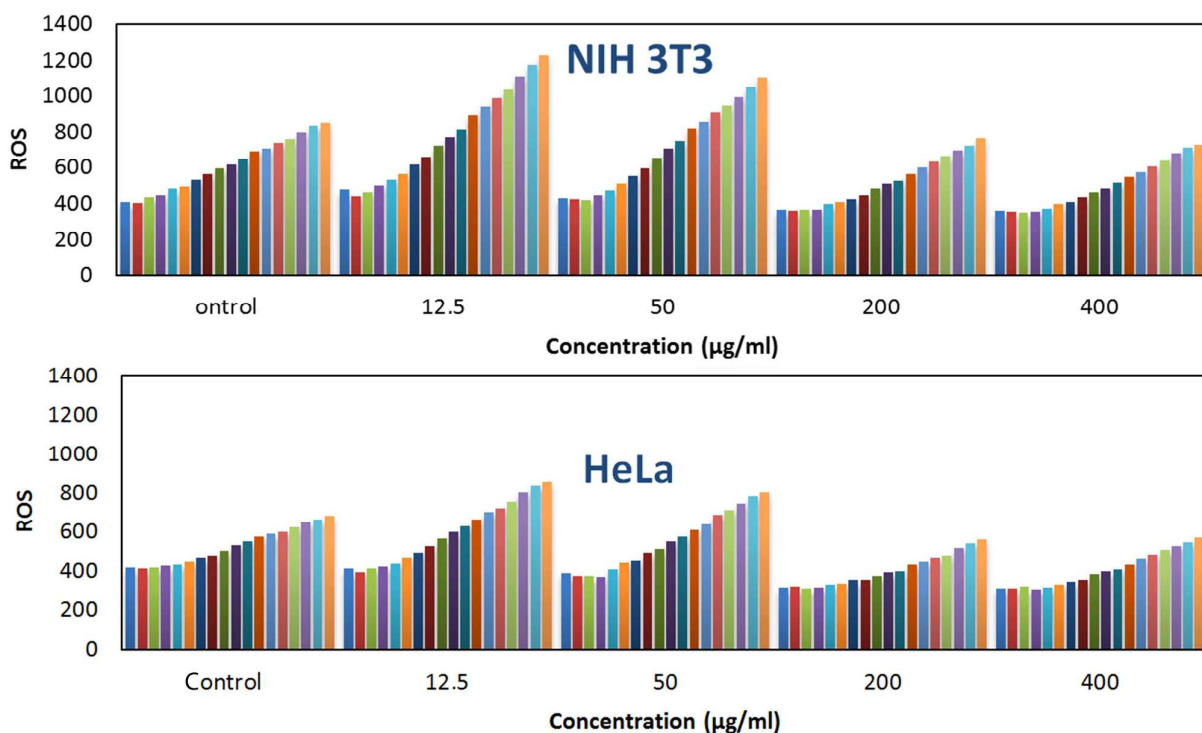


Figure S13. Treating NIH3T3 and HeLa cells with G-COOH causes unusually low levels of reactive oxygen species (ROS) production. ROS production in NIH 3T3 cells and HeLa cells was continuously monitored every 10 min for 3 h, after treatment with 12.5, 50, 200 and 400 $\mu\text{g mL}^{-1}$ of G-COOH. The kinetic production of ROS refers to the rate of formation of ROS of peroxy radicals (HOO), hydroxyl radicals (HO), hypochlorous acid (HOCl), and peroxy radicals (ROO). Both cell lines exhibit a time and dose dependent increase in ROS levels for each tested G-COOH concentration, but in general the ROS levels decrease gradually as the G-COOH concentration increases.

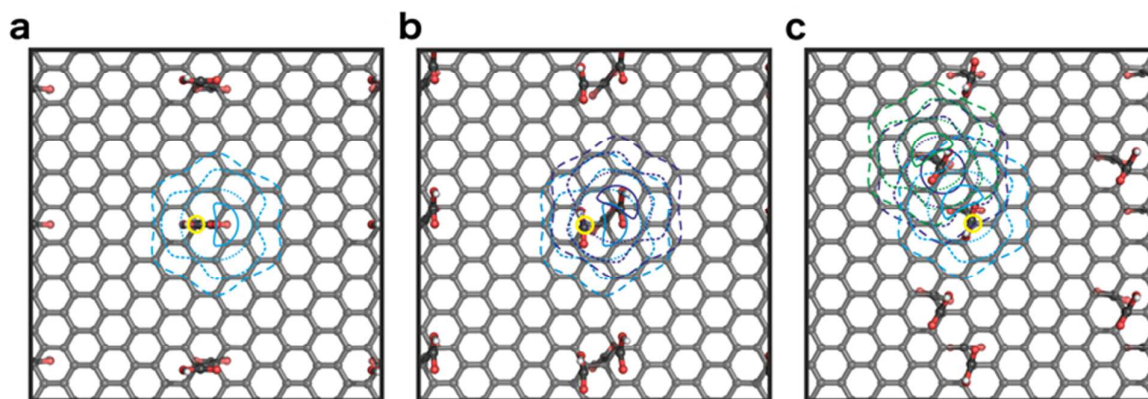


Figure S14. Ground-state (GS) arrangements of G-COOH with the concentration of **a)** 4.2, **b)** 6.3, and **c)** 8.3%. In the search for GS structure, at each coverage the position of one molecule (*e.g.*, marked by yellow circle) was fixed, while the remaining molecules were placed on C atoms marked by lines, which allowed to monitor the total energy changes with the distance between molecules. For clarity, only up to 4 COOH groups per computational cell is displayed. At higher concentration, similar structural motifs are found to be GS arrangements, *i.e.*, the carboxyl groups tended to form chains over the surface (*cf.*, Figure S15 and Figure 5c).

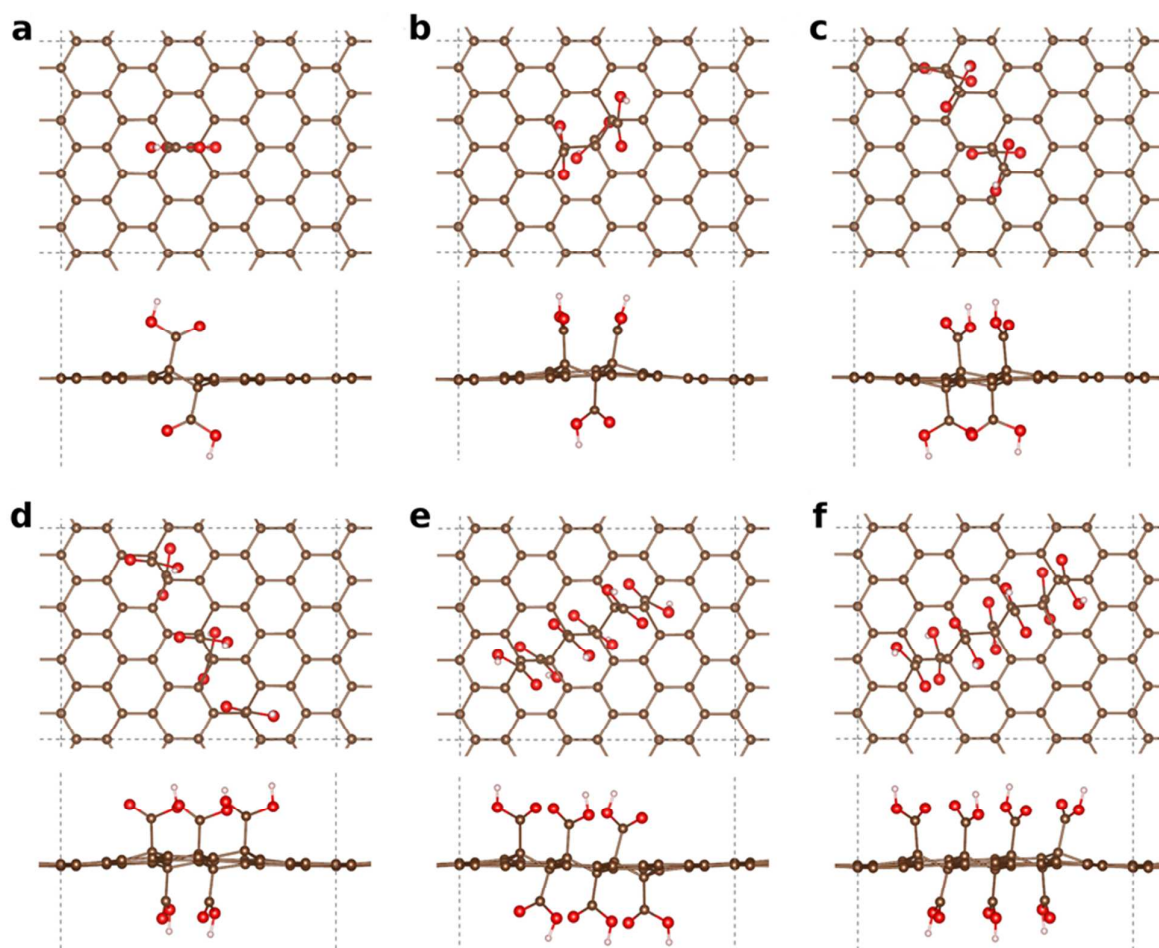


Figure S15. Top-view (upper panels) and side-view (lower panels) of GS arrangements of G-COOH at the concentration of **a)** 4.2, **b)** 6.3, **c)** 8.3, **d)** 10.4, **e)** 12.5, and **f)** 14.6%. Super-cell is marked by dashed lines.

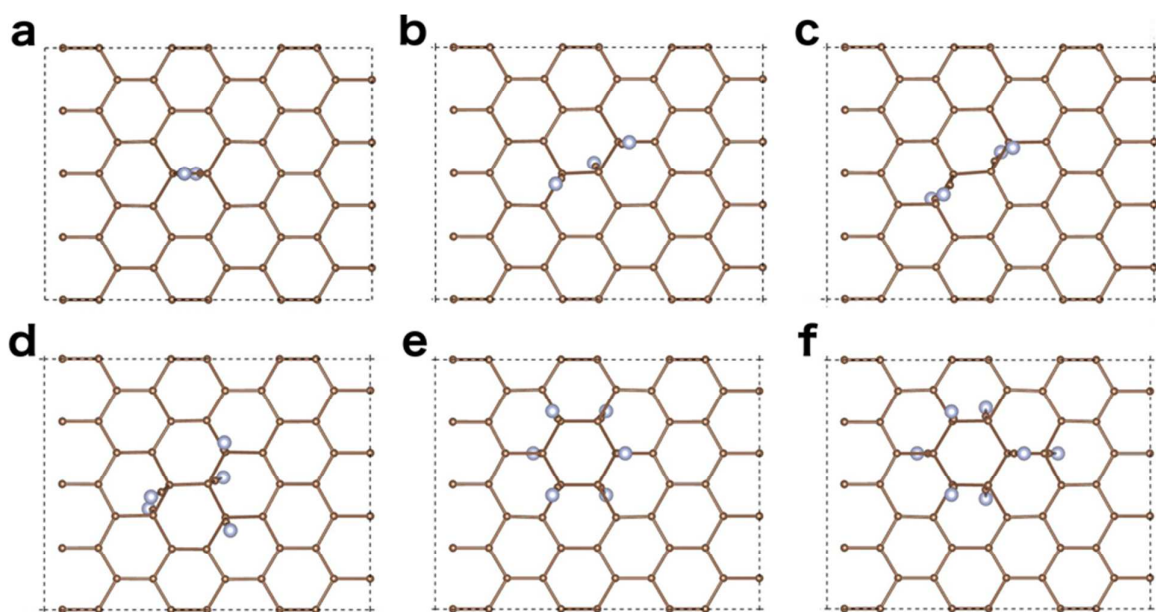


Figure S16. Top-view of GS arrangements of G-CN, *cf.*, Figure S15.

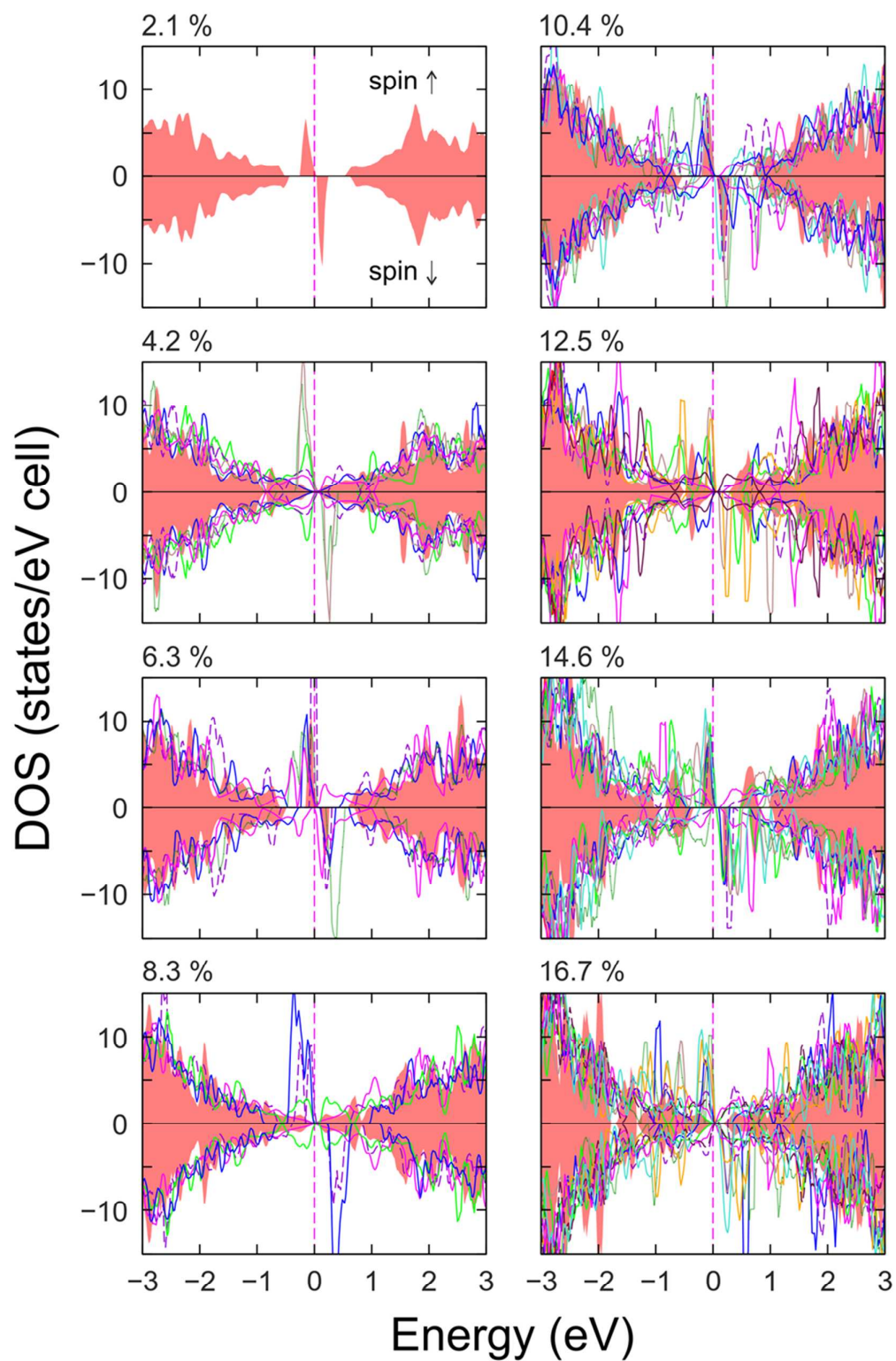


Figure S17. G-COOH DOS profiles assuming degree of functionalization between 2.1 and 16.7%. The DOS plots of GS arrangements are displayed in red. Energy scale is zeroed to E_F and marked by the vertical dashed line.

Supplementary References

- (1) Szabó, T.; Berkesi, O.; Forgó, P.; Josepovits, K.; Sanakis, Y.; Petridis, D.; Dékány, I. Evolution of Surface Functional Groups in a Series of Progressively Oxidized Graphite Oxides. *Chem. Mater.* **2006**, *18*, 2740–2749.
- (2) Bisquert, J.; Garcia-Belmonte, G.; Bueno, P.; Longo, E.; Bulhões, L. O. S. Impedance of Constant Phase Element (CPE)-Blocked Diffusion in Film Electrodes. *J. Electroanal. Chem.* **1998**, *452*, 229–234.
- (3) Jorcin, J.-B.; Orazem, M. E.; Pebere, N.; Tribollet, B. CPE Analysis by Local Electrochemical Impedance Spectroscopy. *Electrochim. Acta* **2006**, *51*, 1473–1479.
- (4) Perdew, J. P.; Burke, K.; Ernzerhof, M. Generalized Gradient Approximation Made Simple. *Phys. Rev. Lett.* **1996**, *77*, 3865–3868.
- (5) Blöchl, P. E. Projector Augmented-Wave Method. *Phys. Rev. B* **1994**, *50*, 17953–17979.
- (6) Kresse, G.; Joubert, D. From Ultrasoft Pseudopotentials to the Projector Augmented-Wave Method. *Phys. Rev. B*, **1999**, *59*, 1758–1775.
- (7) Kresse, G.; Furthmüller, J. Efficiency of Ab-Initio Total Energy Calculations for Metals and Semiconductors Using a Plane-Wave Basis Set. *Comput. Mater. Sci.* **1996**, *6*, 15–50.
- (8) Van Der Spoel, D.; Lindahl, E.; Hess, B.; Groenhof, G.; Mark, A. E.; Berendsen, H. J. C. GROMACS: Fast, Flexible, and Free. *J. Comput. Chem.* **2005**, *26*, 1701–1718.
- (9) Cheng, A.; Steele, W. A. Computer Simulation of Ammonia on Graphite. I. Low Temperature Structure of Monolayer and Bilayer Films. *J. Chem. Phys.* **1990**, *92*, 3858–3866.
- (10) Berendsen, H. J. C.; Grigera, J. R.; Straatsma, T. P. The Missing Term in Effective Pair Potentials. *J. Phys. Chem.* **1987**, *91*, 6269–6271.
- (11) Bussi, G.; Donadio, D.; Parrinello, M. Canonical Sampling Through Velocity Rescaling. *J. Chem. Phys.* **2007**, *126*, 014101.
- (12) Berendsen, H. J. C.; Postma, J. P. M.; van Gunsteren, W. F.; DiNola, A.; Haak, J. R. Molecular Dynamics with Coupling to an External Bath. *J. Chem. Phys.* **1984**, *81*, 3684–3690.
- (13) Hess, B.; Bekker, H.; Berendsen, H. J. C.; Fraaije, J. G. E. M. LINCS: A Linear Constraint Solver for Molecular Simulations. *J. Comput. Chem.* **1997**, *18*, 1463–1472.
- (14) Bayly, C. I.; Cieplak, P.; Cornell, W.; Kollman, P. A. A Well-Behaved Electrostatic Potential Based Method Using Charge Restraints for Deriving Atomic Charges: The RESP Model. *J. Phys. Chem.* **1993**, *97*, 10269–10280.
- (15) Schrodinger, L. L. C. (2015). The PyMOL Molecular Graphics System, Version 1.8.
- (16) Wang, X.; Wang, W.; Liu, Y.; Ren, M.; Xiao, H.; Liu, X. Controllable Defluorination of Fluorinated Graphene and Weakening of C–F Bonding under the Action of Nucleophilic Dipolar Solvent. *Phys. Chem. Chem. Phys.* **2016**, *18*, 3285–3293.
- (17) Lomeda, J. R.; Doyle, C. D.; Kosynkin, D. V.; Hwang, W.-F.; Tour, J. M. Diazonium Functionalization of Surfactant-Wrapped Chemically Converted Graphene Sheets. *J. Am. Chem. Soc.* **2008**, *130*, 16201–16206.
- (18) Zhong, X.; Jin, J.; Li, S.; Niu, Z.; Hu, W.; Li, R.; Ma, J. Aryne Cycloaddition: Highly Efficient Chemical Modification of Graphene. *Chem. Commun.* **2010**, *46*, 7340–7342.
- (19) Quintana, M.; Spyrou, K.; Grzelczak, M.; Browne, W. R.; Rudolf, P.; Prato, M. Functionalization of Graphene via 1,3-Dipolar Cycloaddition. *ACS Nano* **2010**, *4*, 3527–3533.
- (20) Strom, T. A.; Dillon, E. P.; Hamilton, C. E.; Barron, A. R. Nitrene Addition to Exfoliated Graphene: A One-Step Route to Highly Functionalized Graphene. *Chem. Commun.* **2010**, *46*, 4097–4099.
- (21) Economopoulos, S. P.; Rotas, G.; Miyata, Y.; Shinohara, H.; Tagmatarchis, N. Exfoliation and Chemical Modification Using Microwave Irradiation Affording Highly Functionalized Graphene. *ACS Nano* **2010**, *4*, 7499–7507.
- (22) Englert, J. M.; Dotzer, C.; Yang, G.; Schmid, M.; Papp, C.; Gottfried, J. M.; Steinrück, H.-P.; Spiecker, E.; Hauke, F.; Hirsch, A. Covalent Bulk Functionalization of Graphene. *Nat. Chem.* **2011**, *3*, 279–286.
- (23) Bian, S.; Scott, A. M.; Cao, Y.; Liang, Y.; Osuna, S.; Houk, K. N.; Braunschweig, A. B. Covalently Patterned Graphene Surfaces by a Force-Accelerated Diels–Alder Reaction. *J. Am. Chem. Soc.* **2013**, *135*, 9240–9243.
- (24) Englert, J. M.; Vecera, P.; Knirsch, K. C.; Schäfer, R. A.; Hauke, F.; Hirsch, A. Scanning-Raman-Microscopy for the Statistical Analysis of Covalently Functionalized Graphene. *ACS Nano* **2013**, *7*, 5472–5482.
- (25) Zhu, Y.; Higginbotham, A. L.; Tour, J. M. Covalent Functionalization of Surfactant-Wrapped Graphene Nanoribbons. *Chem. Mater.* **2009**, *21*, 5284–5291.
- (26) Dubey, G.; Urcuyo, R.; Abb, S.; Rinke, G.; Burghard, M.; Rauschenbach, S.; Kern, K. Chemical Modification of Graphene via Hyperthermal Molecular Reaction. *J. Am. Chem. Soc.* **2014**, *136*, 13482–13485.
- (27) Borden, W. T.; Gritsan, N. P.; Hadad, C. M.; Karney, W. L.; Kemnitz, C. R.; Platz, M. S. The Interplay of Theory and Experiment in the Study of Phenyl Nitrene. *Acc. Chem. Res.* **2000**, *33*, 765–771.
- (28) Park, J.; Yan, M. Covalent Functionalization of Graphene with Reactive Intermediates. *Acc. Chem. Res.* **2013**, *46*, 181–189.